2020 SCEC Report

Offshore fault damage zones in 3D with Active Source Seismic Data

Abstract: Damage zones can observationally link earthquake physics to mechanics beyond elasticity. The extent of distributed damage affects earthquake rupture propagation, its associated strong motion, and perhaps even the distribution of seismicity around the fault. There are very few 3D observations of damage. Here we constrain the Palos Verdes Fault damage zone offshore California using existing 3D seismic reflection datasets. We use a novel algorithm to identify faults and fractures in a large seismic volume consisting of 4.8×10^8 points and examine the spatial distribution of damage. Our results from the Palo Verdes Fault Zone show that damage is focused around mapped faults and that damage decays with distance from the fault, reaching the undisturbed and mostly unfractured background at a distance of 2.2 km from the fault. The identified damaged zone appears to obey power law behavior at the outer edges of a 3 strand fault network, with a power law exponent of 0.68, this trend extrapolates to a probability of 1 at the mapped fault location. The power law like scaling of apparent fractures with distance from fault is striking similar to outcrop studies, but extends to distances seldom accessible. We find that fracturing in the damage zone increases with depth to around 500 m and at greater depths may be more strongly controlled by lithological grain size, induration, and unit thickness.

1. Introduction

Earthquakes release accumulated strain energy. How the released energy is partitioned during rupture controls propagation and sets the boundary conditions for subsequent events. Energy absorbed in damage zones around faults is a vital sink of strain energy sink and estimates vary widely. Damage zones are highly permeable and particularly important to the distribution and mobility of fluids around faults. The damage zone is the area where fracture density is higher than the surrounding background fracture density. A fault zone consists of a highly localized principal slip surface of highly comminuted granular clay rich gouge material (Chester and Logan, 1986; Chester et al., 1986; Caine et al., 1996; Choi et al., 2016). The principal slip surface is thought to accommodate the majority of the displacement and fault slip. The slip surface is bound on either side by cataclasite grading to breccias which transitions into a tabular damage zone at greater distances. The damage zone experiences less intense deformation compared to fault core and is thought to be related to crack tip propagation or the cumulative wearing effect of repeated ruptures. (Cowie and Shipton, 1998; Scholz et al., 1993).

Basic knowledge of the systematics of damage zones is limited, and most of what we know about damage zones is based on geologic outcrop exposures and related observations (Keren & Kirkpatrick, 2016; Mitchell & Faulkner, 2009; Savage & Brodsky, 2011; Scholz et al., 1993; Shipton et al., 2006; Wilson et al., 2003). Outcrop studies of damage zones typically consist of quantifying cracks surrounding the principal slip surface and identify the damage zone as the area where cracks are more abundant than the background. In these studies the damage zone width has been shown to scale with various fault parameters such as length, displacement, and number of strands. (Torabi and Berg, 2011; Childs et al., 1997). Faults at field and laboratory scales are observed to be complex and may vary in response to repeated slip events. The damage zone plays a role in rupture and perhaps nucleation (Ben-Zion and Zaliapin, 2020;

Cartwright-Taylor et al., 2020). Outcrop studies have been largely limited to surficial measurements of fracture density and lacked the means to quantify the damage in situ at depth. In particular, it has been difficult to address fundamental questions of how depth, lithology and stress regime control the spatial systematics of the damage zone.

Seismic data has contributed to our understanding of fault damage zones in-situ as a sampling of the distinct elastic material properties that are sampled passively with seismic waves (Ben-Zion et al., 2003; Cochran et al., 2009; Vidale & Li, 2003). Passive seismic experiments and techniques are limited by access and deployment logistics on land. Active source marine seismic data may provide a means to improve the situation and provide a higher-resolution and more robust image of the subsurface. 3D Seismic reflection techniques, typically used in hydrocarbon exploration, have the capability of observing fault and fracture networks in-situ. Access to high cost and often proprietary 3D datasets is limited and have only recently been utilized in academic studies (Alaei and Torabi, 2017; Iacopini et al., 2016; Torabi et al., 2017). Here we use 3D seismic data along with an algorithm to extract a fault network from the data. We compare the algorithmically identified faults and fractures to manually mapped 3D fault surfaces. We identify and image the damage zone, identify the spatial decay of damage with distance from the fault surface, as well as analyze the depth, lithology, unit thickness impact on damage.

2 Data

The Palos Verdes Fault (PVF) is located primarily offshore Southern California in the Inner Continental Borderlands, and is an active constituent of the distributed shear zone that is accommodating relative motion between the Pacific and North American Plates (Figure 1). Current estimates suggest that the borderlands accommodates 6 - 8 mm/yr of right lateral motions, accounting for about 15% of the motion across the entire shear zone. The PVF has one of the highest slip rates in Southern California, with estimated rates between 1.9 - 4 mm / yr (Ward and Valensise, 1994; McNeilen et al., 1996; Brankman and Shaw, 2009; Brothers et al., 2015).

In order to examine the damage zone in-situ we utilize existing marine seismic reflection data that is openly available through the USGS at the National Archive of Marine Seismic Surveys. We utilize two overlapping legacy industry collected 3D marine seismic reflection datasets along with 2D multi-channels seismic surveys collected offshore of Los Angeles over the San Pedro shelf and slope, spanning ~20 km of the PVF (Figure 1). The larger of the two volumes has a 346 km^2 footprint and was collected by Chevron in 1976 (C-01-76SC-3D). In addition we used the smaller, higher resolution, smaller binspacing, and more modern dataset collected by Shell in 1984 (B-388-84SC-3D). In support of the 3D seismic data we use 2D airgun and sparker sourced multi-channel seismic lines that intersect the 3D volumes as well as Beta field exploratory geophysical well logs. We also used exploratory geophysical well log and lithology logs to create a 1D velocity model for the volume, allowing the conversion of the time volume to depth.

3 Methods

3.1 Data Conditioning

This section describes the methods and workflow outlined schematically in Figure 2a. First, downloaded data navigation headers were converted from North American Datum 1927 (NAD27) to Universal Transverse Mercator 11 N and imported into seismic interpretation software, OpenDTect, where conditioning of the data included dip-steered diffusion filtering to reduce noise and increase lateral continuity of geologic reflectors. The attribute applies median filtering in a moving 3D window (inline, cross-line, time-window) following structural dip in areas shallow to moderate dips. Areas with very steep dips are not median filtered which reduces smearing of median filtering across faulting discontinuities (Marfurt et al.,1998; Tingdhal and de Rooij, 2003).

3.2 Manual Fault Mapping

Three traces of the fault were manually mapped through the volume in the sedimentary section. We chose to confine our study and mapping to the sedimentary strata where the fault could be mapped continuously and with confidence (250 m - 2.2 km). We avoided the chaotic reflection character of the basement (depth > 2.2 km) and the clear processing artifacts in the shallow section (depth < 250 m). Three continuous PVF fault stands were mapped through the majority of the larger volume (Figure 1). The existence of three PVF strands is consistent with USGS offshore mapping efforts (Walton et al., 2002; Conrad et al., 2010). The 3D fault picks were interpolated forming 3D fault surfaces.

3.3 Automated Fault Detection

We use the ‘thinned fault likelihood’ algorithm to automate identification of smaller faults and fractures within the volume (Hale, 2012 & 2013), which is shown in cartoon form on Figure 2. This method uses semblance (a measure of multitrace similarity over a time-window) to scan adjacent traces to identify discontinuous regions, over a moving window (Figure 2.b). The local maxima of the calculation are preserved, effectively thinning the discontinuity volume (Figure 2c). The discontinuous voxels are then scanned over geologically reasonable dips and azimuths for adjacent voxels of high fault likelihood which are then linked together to form a fault and fracture network. For example of the results of thinned fault likelihood see Figure 3. The thinned fault likelihood attribute volume has a probability for each voxel in 3D space being a fault or fracture.

4. Measuring Damage as a Function of Distance for the Fault

To examine how fracturing varies spatially with respect to the center of the fault zone, we calculate the minimum distance from each voxel (N = 4.8 x 10^8) in the volume to the manually mapped and interpolated central fault strand surface (N = 2 x 10^6). We focus our study on the

eastern side of the central fault strand where the reflectors are more horizontal and less undeformed. Similar to manual fault mapping we limit our analysis to depths below the processing artifacts (>250 m) and above the basement (< 2.2 km) consisting of the Cretaceous Catalina Schist fm. which is highly scattering producing spurious thinned fault likelihood probabilities. We bin the data spatially both by distance from fault and depth in order and calculate the arithmetic mean probability per spatial bin to examine spatial relationships of thinned fault likelihood probability.

First, we analyze the resulting average probabilities <P> as a function of distance from the fault (Figure 3). There is a clear relationship between fracture probability and lateral distance from the fault that decays to a stable background value. This data appears to obey a power law over a limited distance range (between the eastern strand to background), and can be well represented by,

$$\langle P(x) \rangle = Cx^m$$

where x is the perpendicular distance from the fault surface, C is a constant the slope m is -0.68 +/- 0.02. At distances less than 150 meters we suspect that the fracture probability measure is saturated. We speculate that the power law may be extrapolated back to the distance where fracture probability value of 1 which occurs at ~ 10 meters from the fault surface.

Next, we investigate the impact of lithology and depth on damage. We calculate fracture probability for each sample depth. We classify the data to within the bounds of the inner fault damage zone where the fault probability measure is not saturated and background fracture density (2.5 - 6 km) which is easily observable as the horizontal portion of Figure 4, and indicated in Figure 3. We perform a simple subtraction of the depth dependent fracture probability of the fault zone from the background to account for geometric spreading, intrinsic attenuation, and reduce resolvability with depth inherent to active source seismic imaging. The result is shown in Figure 5, and lithological tops are indicated, which are calculated as the mean depth from lithology logs in the beta field. Note that all rock types here are sedimentary, and that the boundaries represent disconformities. The results here show that deeper than about 500 m that the units may be the most significant control on fracturing.

5 Results and Discussion

5.1 Density - Distance Relationship and Fault-bounded damage zones

The thinned fault likelihood method appears to be successfully identifying faults and fractures within the seismic volume. The attribute identifies features within the data that seismic interpreters would likely identify as a fault such as offset in reflector and changes in reflection characteristics. Additionally, the areas with the highest probability for fracture identified by the attribute are localized around faults identified in this study and others as the Palos Verdes Fault

and Wilmington Fault (eastern edge of volume) (Brankman and Shaw, 2009; Conrad et al., 2007; Sorlien et al., 2013, Thompson et al., 2015; Wolfe et al., 2019).

We find that the fracture probability dependance on distance from the center strand of the fault is best fit by a power law relationship, with a power-law exponent of 0.68. This observation is of the same functional form as those observed in outcrop studies (Chester and Logan, 1986; Micarelli et al., 2003; Berg and Skar, 2005; Savage and Brodsky, 2011);. however, some studies have preferred an exponential decay form. (Faulkner et al., 2003; Mitchell and Faulkner, 2009). Bonnet et al. in 2001 explained that distinguishing exponential and power-laws relationships may not be straightforward and that it is advised to span several orders of magnitude before determining the appropriate functional form. This study spans 3 orders of magnitude (50 - 8000 m) in the dataset. Each seismic bin (voxel) has dimensions of 50 m x 25 m x 4 ms (z dimension ~= 5m) and we extend our study to 8 km in distance from the fault, these observations are at distances from the fault that are rarely accessible in outcrop studies. Nearly 2 orders of magnitude are included (450 - 2200 m) when fitting the fracture probability outside the bounds of the mapped fault strands (Figure 4.). Unique to this method and study is the clearly defined edge of the fault zone, where power-law behavior intersects the background at 2.2 km from the central strand (Figure 4.) providing a robust distance cut off for fitting.

The along-strike averaged fracture density, over the depth ranges of 250 - 2200 m depth (nearly seismogenic depths) also has power law scaling. We capture the behavior of the damage zone at large length scales and show that the power law decay relationship extends to at least the 10^3 m length scale. It has been argued that the observation of a broad distributed damage zone is a result of the superposition of multiple sub-parallel faults that accommodate slip (Mitchell and Faulkner, 2009). The cumulative effect of multiple strands results in a wider zone of damage, where multiple fault strands each have their own damage zone. Our data appear to support the fault strand damage zone superposition model, and we find that the inner fault damage bound between the eastern and the western fault strands is the most intense. We suspect that the area closest to the central fault strand may be at the saturation point for the thinned fault likelihood algorithm (0 m from the fault to 150 m (Figure 4.)). In the determination and calculation of thinned fault likelihood space between ‘thinned faults’ is prescribed in the method and 0.12 appears to be the maximum spatially averaged probability within the dataset, however, the large scale aggregate fault appears to follow power law scaling. If we assume that there is no break in the scaling, the fit line may be extrapolated and projected to probability of 1 (highest certainty of fault), corresponding to a distance of ~10 m from the mapped fault surface, which is well within the uncertainty of our mapping and is rather remarkable.

5.2 Damage Zone Width

The data indicates the half width of the Palos Verdes Fault is 2.2 km, or 4.5 km total width. The width determined is indicated by the clear break in slope (Figure 4.) defining a clear boundary between the fault and the relatively undisturbed basin. The width identified here is of the same order as the widths inferred in some passive seismic tomography studies (1 - 2 km) (Thurber et al., 1997; Yang et al., 2011; Cochran et al., 2009). The passive seismic studies hinge on seismic

body wave ray paths to sample the fault zone and thus limited in their resolution and spatial sampling, in contrast to our study has uniform sampling throughout, and may be more resolving of the outer bounds of the damage zone.

5.3 Sedimentary Rock and Damage

We analyze how fracturing and damage evolves with depth (Figure 5.) It appears that fracturing increases slightly with depth for regions within the inner fault bound damage zone at depths less than 500 meters. The progressive increase in fracturing up to 500 meters may be suggestive of gradational diagenetic effects that occur in response to increased pressure and temperature with sediment burial. The background fracture level may decrease slightly with depth, but the signal is too weak (at the lower limit of the study) to interpret and speculate that intrinsic attenuation, fresnel zone, and geometric spreading (which increases with propagation distance / travel time) have an effect on the detection faulting features by the thinned fault likelihood algorithm. Note the stability of the differenced result through the Monterey - Delmontian formations, and the stability of the fracture probability among many of the overlying strata.

6 Conclusions

We find that the damage zone is observable and identifiable in seismic data. The seismic attribute computed from the data is representative of the damage zone and areas with elevated fault and fracture probability are consistent with areas of mapped faults both in this study and independent fault mapping efforts. We find that the level of fracturing scales with lateral distance from the fault. This trend is best fit by a power-law with an exponent of ~0.7 for the regions outside of the mapped fault strands, this scaling relationship is similar to other mature systems. An extrapolation of the power-law fit, projects to a probability of 1 on the central main strand. Due to the large footprint and large amount of data we extend observations to greater distances and with more continuous sampling than is typically done at the outcrop scale. Additionally, the large dataset allows for a well defined background and edge of the damage zone which is ~2.2 km away, and the next fault system creates a clear separate signal. Damage increases moderately with depth to ~500m, beyond which it appears that formation lithology is stronger control on damage.

References:

Alaei, B., & Torabi, A. (2017). Seismic imaging of fault damaged zone and its scaling relation with displacement. Interpretation, 5(4), SP83–SP93. https://doi.org/10.1190/INT-2016-0230.1

Alcalde, J., Bond, C. E., Johnson, G., Ellis, J. F., & Butler, R. W. H. (2017). Impact of seismic image quality on fault interpretation uncertainty. GSA Today. https://doi.org/10.1130/GSATG282A.1

Atwater, T. (1970). Implications of plate tectonics for the Cenozoic tectonic evolution of western North America. Geological Society of America Bulletin, 81(12), 3513-3536.

Behl, R. J. (1999). Since Bramlette (1946): The Miocene Monterey Formation of California revisited. *Classic Cordilleran Concepts: A View from California: Geological Society of America, Special Paper*, *338*, 301-313.

Ben-Zion, Y, & Andrews, D. J. (n.d.). Properties and Implications of Dynamic Rupture along a Material Interface. 10.

Ben-Zion, Yehuda, & Sammis, C. G. (2003). Characterization of Fault Zones. Pure Appl. Geophys., 160, 39.

Berg, S. S., & Skar, T. (2005). Controls on damage zone asymmetry of a normal fault zone: Outcrop analyses of a segment of the Moab fault, SE Utah. Journal of Structural Geology, 27(10), 1803–1822. https://doi.org/10.1016/j.jsg.2005.04.012

Bramlette, M. N. (1946). *The Monterey Formation of California and the origin of its siliceous rocks* (Vol. 212). US Government Printing Office.

Yehuda Ben-Zion, Ilya Zaliapin, Localization and coalescence of seismicity before large earthquakes, Geophysical Journal International, Volume 223, Issue 1, October 2020, Pages 561–583, https://doi.org/10.1093/gji/ggaa315

Bohannon, R. G., & Geist, E. (1998). Upper crustal structure and Neogene tectonic development of the California continental borderland. Geological Society of America Bulletin, 110(6), 779–800. https://doi.org/10.1130/0016-7606(1998)110<0779:UCSANT>2.3.CO;2

Bonnet, E., Bour, O., Odling, N. E., Davy, P., Main, I., Cowie, P., & Berkowitz, B. (2001). Scaling of fracture systems in geological media. Reviews of Geophysics, 39(3), 347–383. https://doi.org/10.1029/1999RG000074

Brankman, C. M., & Shaw, J. H. (2009). Structural Geometry and Slip of the Palos Verdes Fault, Southern California: Implications for Earthquake Hazards. Bulletin of the Seismological Society of America, 99(3), 1730–1745. https://doi.org/10.1785/0120080303

Brothers, D. S., Conrad, J. E., Maier, K. L., Paull, C. K., McGann, M., & Caress, D. W. (2015). The Palos Verdes Fault offshore Southern California: Late Pleistocene to present tectonic geomorphology, seascape evolution, and slip rate estimate based on AUV and ROV surveys. Journal of Geophysical Research: Solid Earth, 120(7), 4734–4758. https://doi.org/10.1002/2015JB011938

Boyd, D. (2020). Characterizing the Geometry, Kinematics, and Potential Connectivity at the Southern Termination of the Palos Verdes Fault (Doctoral dissertation, California State University, Long Beach).

Cartwright-Taylor, A., Main, I. G., Butler, I. B., Fusseis, F., Flynn, M., & King, A. (2020). Catastrophic Failure: How and When? Insights From 4-D In Situ X-ray Microtomography. Journal of Geophysical Research: Solid Earth, 125(8), e2020JB019642.

Caine, J. S., Evans, J. P., & Forster, C. B. (1996). Fault zone architecture and permeability structure. Geology, 24(11), 1025. https://doi.org/10.1130/0091-7613(1996)024<1025:FZAAPS>2.3.CO;2

Chester, F. M., & Logan, J. M. (1986). Implications for mechanical properties of brittle faults from observations of the Punchbowl fault zone, California. Pure and Applied Geophysics PAGEOPH, 124(1–2), 79–106. https://doi.org/10.1007/BF00875720

Childs, C. J. J. P., Walsh, J. J., & Watterson, J. (1997). Complexity in fault zone structure and implications for fault seal prediction. In Norwegian Petroleum Society Special Publications (Vol. 7, pp. 61-72). Elsevier.

Choi, J.-H., Edwards, P., Ko, K., & Kim, Y.-S. (2016). Definition and classification of fault damage zones: A review and a new methodological approach. Earth-Science Reviews, 152, 70–87. https://doi.org/10.1016/j.earscirev.2015.11.006

Cochran, E. S., Li, Y.-G., Shearer, P. M., Barbot, S., Fialko, Y., & Vidale, J. E. (2009). Seismic and geodetic evidence for extensive, long-lived fault damage zones. Geology, 37(4), 315–318. https://doi.org/10.1130/G25306A.1

Conrad, J. E., Paull, C. K., McGann, M. L., Edwards, B. D., Ryan, H. F., Caress, D. W., ... & Lundsten, E. (2010, December). Determination of slip rates for offshore fault zones: An example from the Palos Verdes fault zone, southern California. In AGU Fall Meeting Abstracts (Vol. 2010, pp. T33B-2231).

Crouch, J. K., & Suppe, J. (1993). Late Cenozoic tectonic evolution of the Los Angeles basin and inner California borderland: A model for core complex-like crustal extension. Geological Society of America Bulletin, 105(11), 1415-1434.

Cowie, P. A., & Shipton, Z. K. (1998). Fault tip displacement gradients and process zone dimensions. Journal of Structural Geology, 20(8), 983–997. https://doi.org/10.1016/S0191-8141(98)00029-7

Faulkner, D. R., Lewis, A. C., & Rutter, E. H. (2003). On the internal structure and mechanics of large strike-slip fault zones: Field observations of the Carboneras fault in southeastern Spain. Tectonophysics, 367(3–4), 235–251. https://doi.org/10.1016/S0040-1951(03)00134-3

Fialko, Y. (2002). Deformation on Nearby Faults Induced by the 1999 Hector Mine Earthquake. Science, 297(5588), 1858–1862. https://doi.org/10.1126/science.1074671

Fisher, M. A. (2004). The Offshore Palos Verdes Fault Zone near San Pedro, Southern California. Bulletin of the Seismological Society of America, 94(2), 506–530. https://doi.org/10.1785/0120030042

Gulley, A. K., Eccles, J. D., Kaipio, J. P., & Malin, P. E. (2017). The effect of gradational velocities and anisotropy on fault-zone trapped waves. Geophysical Journal International, 210(2), 964–978. https://doi.org/10.1093/gji/ggx200

Hale, D. (2013). Methods to compute fault images, extract fault surfaces, and estimate fault throws from 3D seismic images. GEOPHYSICS, 78(2), O33–O43. https://doi.org/10.1190/geo2012-0331.1

Heynekamp, M. R., Goodwin, L. B., Mozley, P. S., & Haneberg, W. C. (1999). Controls on fault-zone architecture in poorly lithified sediments, Rio Grande Rift, New Mexico: Implications for fault-zone permeability and fluid flow. In W. C. Haneberg, P. S. Mozley, J. C. Moore, & L. B. Goodwin (Eds.), Geophysical Monograph Series (Vol. 113, pp. 27–49). American Geophysical Union. https://doi.org/10.1029/GM113p0027

Hubbard, J., Shaw, J. H., Dolan, J., Pratt, T. L., McAuliffe, L., & Rockwell, T. K. (2014). Structure and Seismic Hazard of the Ventura Avenue Anticline and Ventura Fault, California: Prospect for Large, Multisegment Ruptures in the Western Transverse Ranges. Bulletin of the Seismological Society of America, 104(3), 1070–1087. https://doi.org/10.1785/0120130125

Iacopini, D., Butler, R. W. H., Purves, S., McArdle, N., & De Freslon, N. (2016). Exploring the seismic expression of fault zones in 3D seismic volumes. Journal of Structural Geology, 89, 54–73. https://doi.org/10.1016/j.jsg.2016.05.005

Keren, T. T., & Kirkpatrick, J. D. (2016). The damage is done: Low fault friction recorded in the damage zone of the shallow Japan Trench décollement. Journal of Geophysical Research: Solid Earth, 121(5), 3804–3824. https://doi.org/10.1002/2015JB012311

Lewis, M. A., & Ben-Zion, Y. (2010). Diversity of fault zone damage and trapping structures in the Parkfield section of the San Andreas Fault from comprehensive analysis of near fault seismograms: Diversity of fault zone damage at Parkfield. Geophysical Journal International, 183(3), 1579–1595. https://doi.org/10.1111/j.1365-246X.2010.04816.x

Li, S., Freymueller, J., & McCaffrey, R. (2016). Slow slip events and time-dependent variations in locking beneath Lower Cook Inlet of the Alaska-Aleutian subduction zone. Journal of Geophysical Research: Solid Earth, 121(2), 1060–1079. https://doi.org/10.1002/2015JB012491

Li, Y.-G., Ellsworth, W. L., Thurber, C. H., Malin, P. E., & Aki, K. (n.d.). Fault-Zone Guided Waves from Explosions in the San Andreas Fault at Parkfield and Cienega Valley, California. 12.

Li, Y.-G., Vidale, J. E., & Cochran, E. S. (2004). Low-velocity damaged structure of the San Andreas Fault at Parkfield from fault zone trapped waves: LOW-VELOCITY DAMAGED STRUCTURE OF THE SAN ANDREAS FAULT. Geophysical Research Letters, 31(12), n/a-n/a. https://doi.org/10.1029/2003GL019044

Marfurt, K. J., Kirlin, R. L., Farmer, S. L., & Bahorich, M. S. (1998). 3-D seismic attributes using a semblance-based coherency algorithm. GEOPHYSICS, 63(4), 1150–1165. https://doi.org/10.1190/1.1444415

McNeilan, T. W., Rockwell, T. K., & Resnick, G. S. (1996). Style and rate of Holocene slip, Palos Verdes fault, southern California. Journal of Geophysical Research: Solid Earth, 101(B4), 8317–8334. https://doi.org/10.1029/95JB02251

Mitchell, T. M., & Faulkner, D. R. (2009). The nature and origin of off-fault damage surrounding strike-slip fault zones with a wide range of displacements: A field study from the Atacama fault system, northern Chile. Journal of Structural Geology, 31(8), 802–816. https://doi.org/10.1016/j.jsg.2009.05.002

Plesch, A., Shaw, J. H., Benson, C., Bryant, W. A., Carena, S., Cooke, M., ... & Yeats, R. (2007). Community fault model (CFM) for southern California. Bulletin of the Seismological Society of America, 97(6), 1793-1802.

Redin, T. (1991). Oil and Gas Production from Submarine Fans of the Los Angeles Basin: Chapter 8.

Savage, H. M., & Brodsky, E. E. (2011). Collateral damage: Evolution with displacement of fracture distribution and secondary fault strands in fault damage zones. Journal of Geophysical Research, 116(B3). https://doi.org/10.1029/2010JB007665

Scholz, C. H., Dawers, N. H., Yu, J.-Z., Anders, M. H., & Cowie, P. A. (1993). Fault growth and fault scaling laws: Preliminary results. Journal of Geophysical Research: Solid Earth, 98(B12), 21951–21961. https://doi.org/10.1029/93JB01008

Shaw, J. H., & Suppe, J. (1996). Earthquake hazards of active blind-thrust faults under the central Los Angeles basin, California. Journal of Geophysical Research: Solid Earth, 101(B4), 8623–8642. https://doi.org/10.1029/95JB03453

Shipton, Z. K., Soden, A. M., Kirkpatrick, J. D., Bright, A. M., & Lunn, R. J. (2006). How thick is a fault? Fault displacement-thickness scaling revisited. In R. Abercrombie, A. McGarr, H. Kanamori, & G. Di Toro (Eds.), Geophysical Monograph Series (Vol. 170, pp. 193–198). American Geophysical Union. https://doi.org/10.1029/170GM19

Sorlien, C. C., Seeber, L., Broderick, K. G., Luyendyk, B. P., Fisher, M. A., Sliter, R. W., & Normark, W. R. (2013). The Palos Verdes anticlinorium along the Los Angeles, California coast: Implications for underlying thrust faulting: PALOS VERDES ANTICLINORIUM CALIFORNIA. Geochemistry, Geophysics, Geosystems, 14(6), 1866–1890. https://doi.org/10.1002/ggge.20112

Tingdahl, K. M., & de Groot, P. F. (2003). Post-stack dip-and azimuth processing. Journal of Seismic Exploration, 12(2), 113-126.

Thompson, M. A. (2015). Tectonic evolution of the Palos Verdes Fault near Lasuen Knoll, offshore southern California. California State University, Long Beach.

Torabi, A., Alaei, B., & Kolyukhin, D. (2017). Analysis of fault scaling relations using fault seismic attributes: Analysis of fault scaling relations. Geophysical Prospecting, 65(2), 581–595. https://doi.org/10.1111/1365-2478.12440

Torabi, A., & Berg, S. S. (2011). Scaling of fault attributes: A review. Marine and Petroleum Geology, 28(8), 1444–1460. https://doi.org/10.1016/j.marpetgeo.2011.04.003

Vidale, J. E., & Li, Y.-G. (2003). Damage to the shallow Landers fault from the nearby Hector Mine earthquake. Nature, 421(6922), 524–526. https://doi.org/10.1038/nature01354

Walton, M.A.L., Papesh, A.G., Johnson, S.Y., Conrad, J.E., and Brothers, D.S., 2020, Quaternary faults offshore of California: U.S. Geological Survey data release, https://doi.org/10.5066/P91RYEZ4.

Ward, S. N., & Valensise, G. (1994). The Palos Verdes terraces, California: Bathtub rings from a buried reverse fault. Journal of Geophysical Research: Solid Earth, 99(B3), 4485–4494. https://doi.org/10.1029/93JB03362

Webb, T. H., & Kanamori, H. (1985). EARTHQUAKE FOCAL MECHANISMS IN THE EASTERN TRANSVERSE RANGES AND SAN EMIGDIO MOUNTAINS, SOUTHERN CALIFORNIA AND EVIDENCE FOR A REGIONAL DECOLLEMENT. 21.

Wilson, J. E., Chester, J. S., & Chester, F. M. (2003). Microfracture analysis of fault growth and wear processes, Punchbowl Fault, San Andreas system, California. Journal of Structural Geology, 25(11), 1855–1873. https://doi.org/10.1016/S0191-8141(03)00036-1

Wolfe, F. D., Shaw, J. H., Plesch, A., Ponti, D. J., Dolan, J. F., & Legg, M. R. (2019). The Wilmington Blind-Thrust Fault: An Active Concealed Earthquake Source beneath Los Angeles, CaliforniaThe Wilmington Blind-Thrust Fault: An Active Concealed Earthquake Source beneath Los Angeles, California. Bulletin of the Seismological Society of America, 109(5), 1890-1906.

Wu, J., Hole, J. A., Snoke, J. A., & Imhof, M. G. (2008). Depth extent of the fault-zone seismic waveguide: effects of increasing velocity with depth. Geophysical Journal International, 173(2), 611-622.

Yang, H., Li, Z., Peng, Z., Ben-Zion, Y., & Vernon, F. (2014). Low-velocity zones along the San Jacinto Fault, Southern California, from body waves recorded in dense linear arrays: Damage zones of the San Jacinto Fault. Journal of Geophysical Research: Solid Earth, 119(12), 8976–8990. https://doi.org/10.1002/2014JB011548

Yang, H., Zhu, L., & Cochran, E. S. (2011). Seismic structures of the Calico fault zone inferred from local earthquake travel time modelling: Seismic structures of the Calico fault zone. Geophysical Journal International, 186(2), 760–770. https://doi.org/10.1111/j.1365-246X.2011.05055.

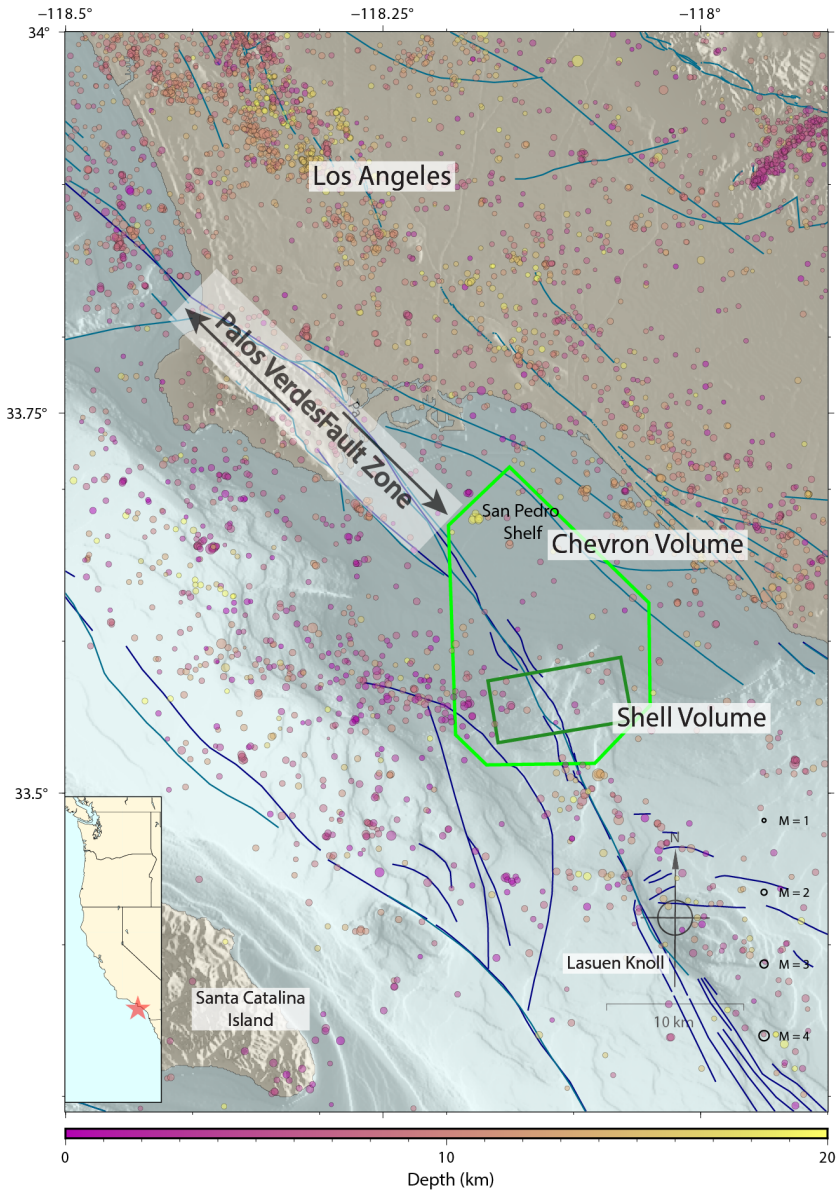

Figure 1: Map of southern california inner borderlands of the San Pedro Shelf. Inset map shows western US, with the red star indicating the region of study area. Main map shows location of mapped fault traces from the USGS quaternary faults database, where the navy blue lines are the USGS offshore quaternary faults dataset and the turquoise lines are the USGS onshore quaternary faults. Thick green polygon indicates the bounds of the 3D marine active source data sets. Circles indicate local earthquakes that are colored according to depth and scaled by magnitude from the Southern California Earthquake Data Center alternate catalog of events included from 1981 - 2018 (Hauksson et al., 2012).

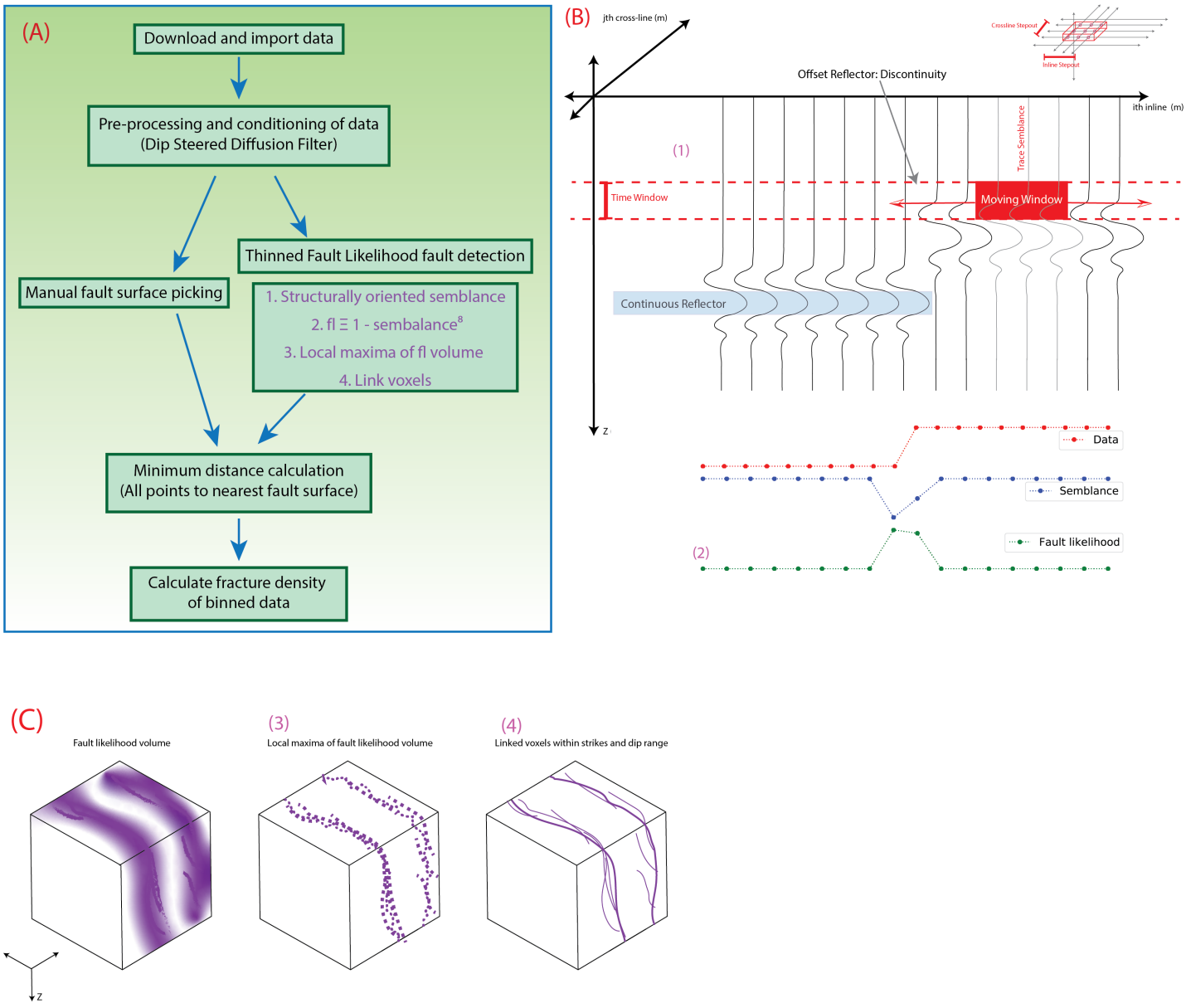

Figure 2. (A) workflow used, where purple numbers in the thinned fault likelihood calculation are shown in cartoon form in B & C. (B) following (Hale, 2013) cartoon showing the fault likelihood volume from a semblance volume where semblance is a measure of multi-trace similarity of adjacent traces over a time window that scans over a moving 3D window that is dip-steered along continuous reflectors. The lower panels depict the fault-likelihood of this moving window cartoon. (C) shows the resulting fault likelihood volume and that the local maxima for fault likelihood is calculated and preserved, thinning the discontinuity volume to areas of highest likelihood for faulting. Finally the thinned discontinuities are linked up forming a fault and fracture network identified purely by the data. For additional description see the Methods section.

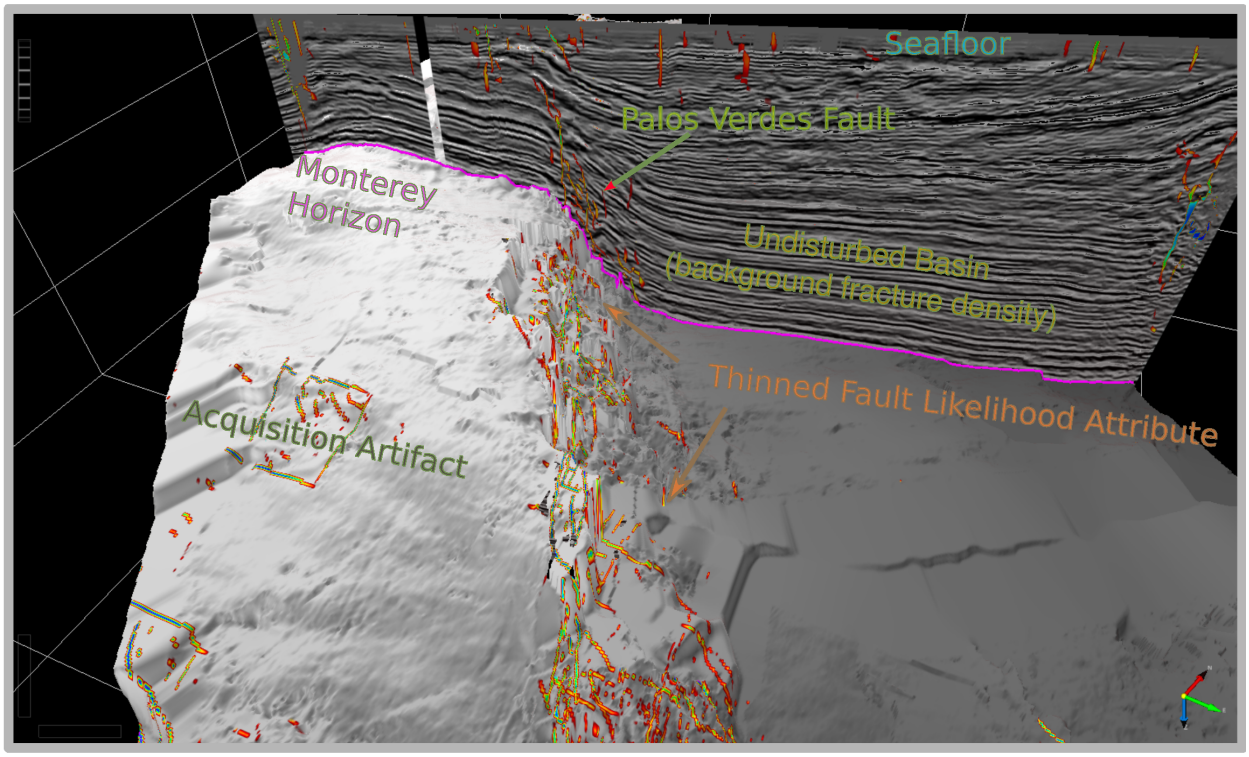

Figure 3. Perspective view of Thinned Fault Likelihood attribute results in high confidence ranges (0.75–1) along the Palos Verdes fault zone. The rainbow colormap ranges from red to violet, where violet is the greatest probability of a fault. The attribute is projected on a strike-perpendicular line and an interpreted and Monterey horizon. Note the variable width of the damage zone along strike, and how the results for thinned fault likelihood are concentrated around the fault.

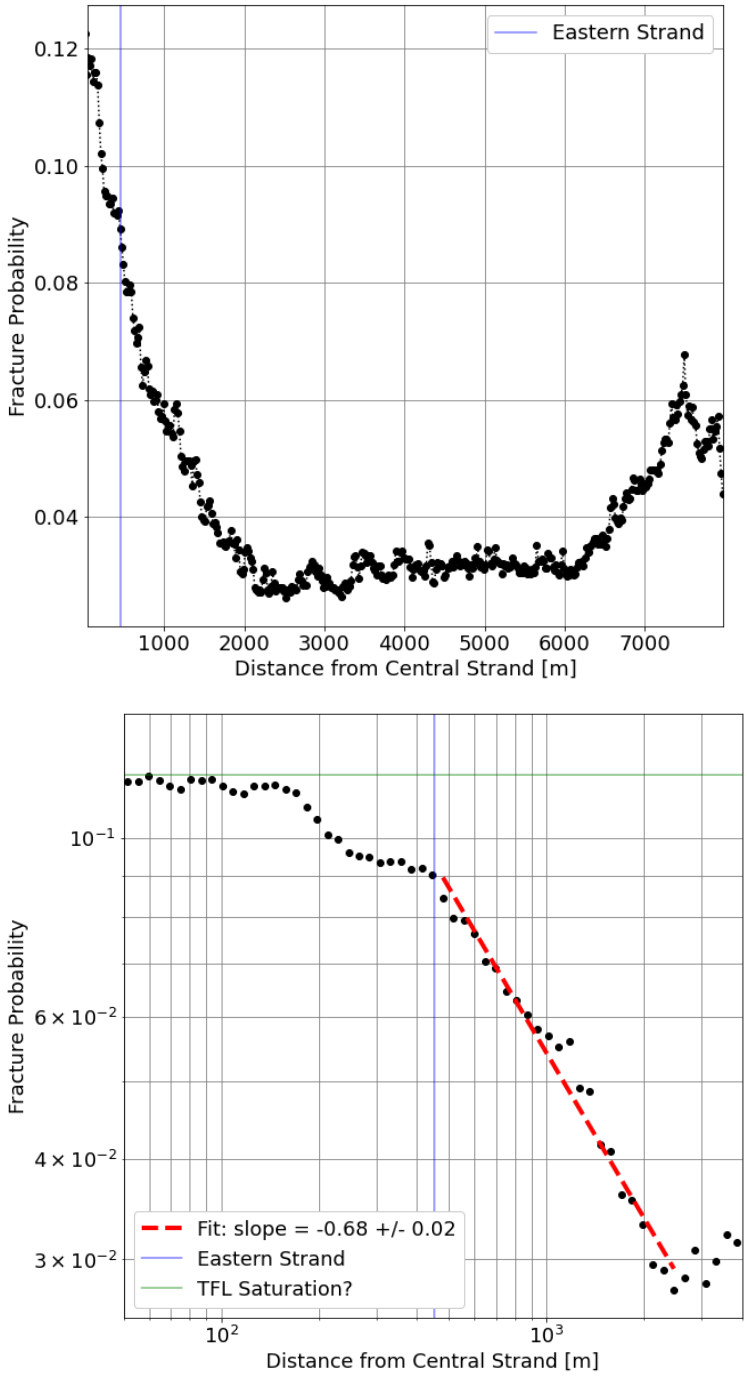

Figure 4. (top) Fracture probability relationship with distance from central mapped strand. Exhibits a decay relationship with increasing distance from the center of the central fault strand. Fracture probability decays with distance from the central strand to ~ 2.2 km from the fault. The background fracture probability extends from 2.2 km to 6.2 km from the fault before fracture increases again, due to the Wilmington fault at the eastern edge of the seismic volume. (bottom) Shows spatial relationship between fracture density and distance from the central strand. Red line indicates least squares power law fit through the data that extends from the bounds of the eastern strand to the background (~ 2.2 km).

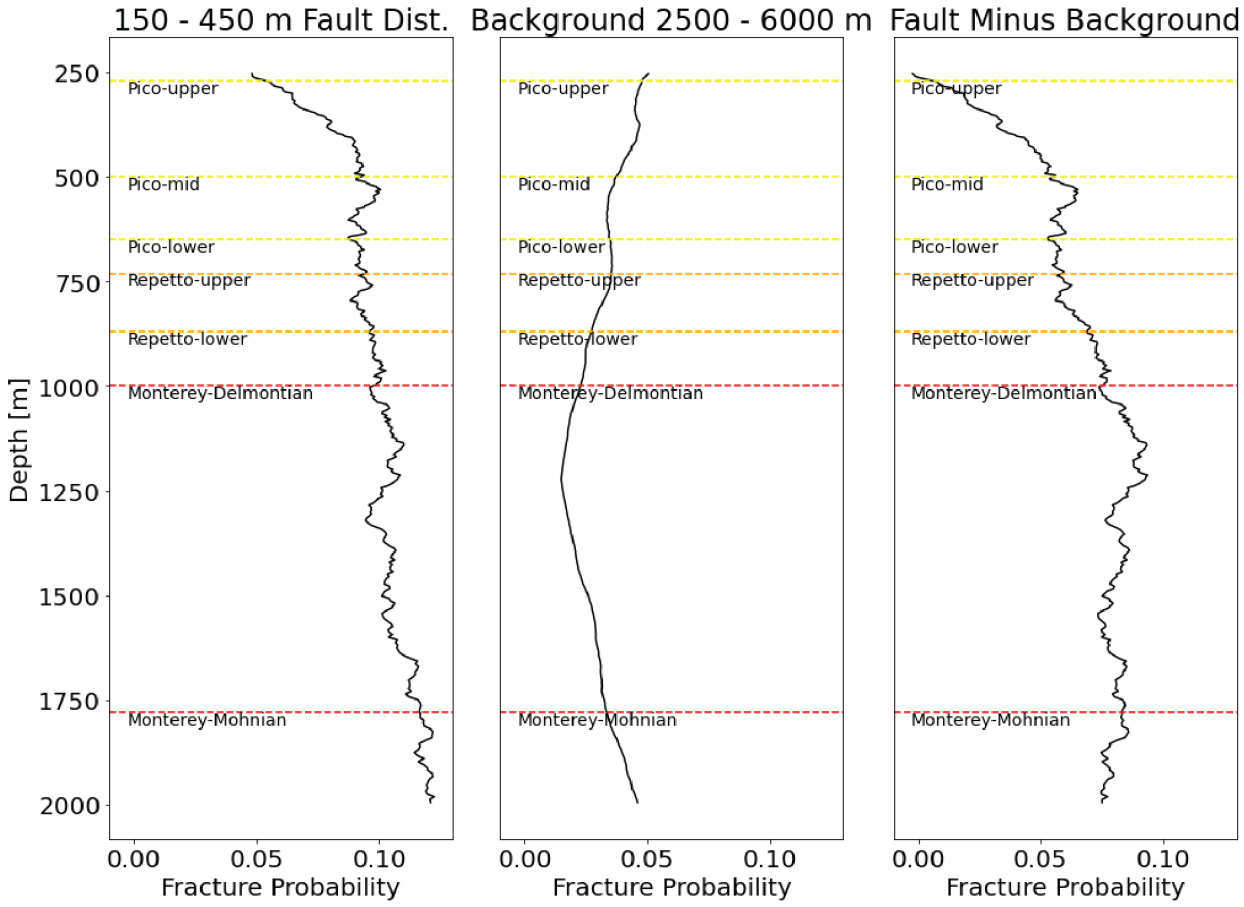

Figure 5. Three panels showing fault probability variation with depth. The mean unit boundary depth as determined by averaging Beta oil field exploratory well log tops. Main units from shallowest to deepest are Pico, Repetto, and Monterey. (left) shows how fracture probability changes with depth within the inner fault bound damage zone, but outside of the region where thinned fault likelihood may be saturated. (center) shows fracture probability relationship with depth for the background region 2.5 - 6 km. (right) shows simple subtraction of the background from the fault. Note the stability within units.